Image Formation in Spectral Computed Tomography

Simon Rit, Cyril Mory, Peter B Noël

Image Formation in Spectral Computed Tomography

S. Rit[1], C. Mory[1] and P.B. Noël[2]

[1]Univ Lyon, INSA-Lyon, Université Claude Bernard Lyon 1, UJM-Saint Etienne, CNRS, Inserm, CREATIS UMR 5220, U1206, F-69373, Lyon, France.
[2]Department of Radiology, Perelman School of Medicine, University of Pennsylvania, Philadelphia, USA.

Spectral Computed Tomography (CT) can perform "color" x-ray detection; for example, photon-counting detectors can discriminate the energy of individual x-ray photons and divide them into several predefined energy bins, thereby providing a spectral analysis of the transmitted x-ray beam. By measuring the x-ray attenuation in two or more distinct energy bins, one can gain information about the elemental composition of an object, making it possible via material decomposition to distinguish between different materials, such as contrast agents and different types of tissues, in a single CT scan. This concept of spectral CT is based on the x-ray attenuation differences of various materials when simultaneously exposed by a spectrum of x-ray photons (which are emitted in a wide spectral range by a standard x-ray tube). Attenuation differences reflect the differences in material interactions with low- and high-energy photons, mainly Compton scatter and photoelectric effects in the diagnostic energy range. Interaction of x-rays with matter is described by the linear attenuation coefficient μ of an object, which depends on the three-dimensional (3D) position $\boldsymbol{x}$ in space and the one-dimensional (1D) energy ϵ of incident photons. The photon fluence Φ after the object of a monoenergetic pencil beam is described by the Beer-Lambert law

$$\Phi = \Phi_0 \exp\left(-\int_{\mathcal{L}} \mu(\boldsymbol{x}, \epsilon)\, \mathrm{d}\ell\right) \tag{1}$$

with ϵ the beam energy, Φ_0 the initial beam fluence, and $\mathcal{L}$ the line corresponding to the beam.

Conventional CT scanners acquire a single sinogram, mixing all photons regardless of their energy. Reconstruction algorithms for single-energy CT either neglect the energy dependency of the incident beam or use corrections for multi-energy effects known as beam hardening [8], for example by assuming that a single material composes the object in the field-of-view [7]. Spectral CT scanners employ a variety of strategies to acquire multiple sinograms representative of different energy segments of the incoming spectra [38]. The purpose of this chapter is to present specific algorithmic solutions required to utilize this additional energy dimension in combination with conventional and advanced tomographic reconstruction algorithms.

The central goal of spectral processing steps is to reconstruct not only a 3D μ map at a given (effective) energy, but a four-dimensional (4D) μ for the energy range measured with two to five energy discrimination measurements provided by a spectral CT scanner. A simplified model becomes necessary and many contributions (also presented in this chapter) are based on a model proposed by Alvarez and Macovski [4]. This paradigm describes μ as a linear combination of a few energy-independent and space-independent functions, which they note

$$\mu(\boldsymbol{x}, \epsilon) \approx \sum_{m=1}^{\mathrm{M}} a_m(\boldsymbol{x}) f_m(\epsilon) \tag{2}$$

with $\boldsymbol{x}$ the 3D position in the object, M the number of basis functions, a_m the 3D space-dependent (but energy-independent) functions, and f_m the energy-dependent (but space-independent) functions. Two approaches have been proposed for the f_m functions and a_m volumes in human tissue. Both methods only require $\mathrm{M} = 2$ basis functions. One is to assume that the object attenuates x-rays as if it was composed of two materials, e.g. water and bone [23]. The function f_m is then the mass-attenuation coefficient of material m, which solely depends on the energy, and the volume a_m is a map of the concentration of material m. The other approach proposes that image contrast is based on an x-ray particle model describing the physical interaction of photoelectric absorption and Compton scattering. The function f_m then approximates the energy dependence of the

phenomenon m, and the volume a_m is a map of the cross-section for that type of interaction. In addition to the two functions to represent human materials, there can be additional components in the basis to represent non-human elements (M > 2), e.g. contrast materials having a K-absorption edge in the diagnostic energy range [57, 82]. Without loss of generality, we will refer to f_m as material specific CT maps in the following sections.

The x-ray source of a CT scanner is polychromatic and characterized by an energy spectrum. Similarly, the signal measured by the detector is a function of the energies of impinging photons. The impinging spectrum is not equivalent to the measured one because the measurements can be distorted while the signal is picked up from the detector and processed by complex electronics. The ratio of the spectrum collected with a detector over the impinging spectrum is called a detector response function or pulse height distribution. These two energy functions can be merged into an *effective spectrum* which is the product of the source spectrum and the detector response function. The concept of an effective spectrum can describe any spectral system, whether several effective spectra are acquired by using different source spectra, e.g. with different source voltages, by using two detectors with different responses, e.g. with different sensitive materials, or by using different energy thresholds for photon counting detectors. Figure 1 illustrates the effective spectra of different systems.

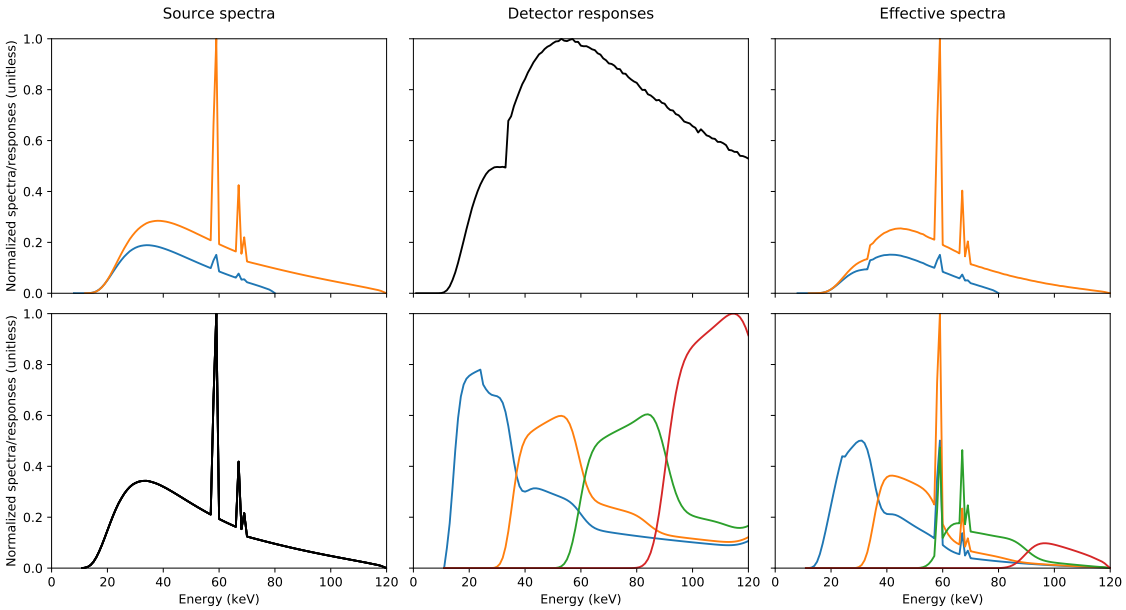

Figure 1: Examples of source spectra (left), detector responses (middle) and effective spectra (right), for a fast-switching x-ray source with an energy-integrating detector with a CsI scintillator (top, data from system #2 in [81]) and a photon-counting system with four energy bins (bottom, data from [16]).

Plugging the model of the linear attenuation coefficient (Equation 2) into the Beer-Lambert law (Equation 1) and accounting for the polychromatism of the effective spectra leads to the forward model of the inverse problem studied in this chapter

$$\hat{y}_{ib} = \int_{\mathbb{R}^+} s_b(\epsilon) \exp\left(- \int_{\mathcal{L}_i} \sum_{m=1}^{\mathrm{M}} a_m(\boldsymbol{x}) f_m(\epsilon) \, \mathrm{d}\ell \right) \mathrm{d}\epsilon \tag{3}$$

with $\hat{y}_{ib}$ the expectation of the measures for the i-th detector pixel and the b-th effective spectrum s_b (b stands for energy bin in photon counting systems). The goal of this inverse problem is to estimate the unknown material images $\boldsymbol{a}$ from measures $\boldsymbol{y}$. The effective spectra s can be estimated independently, before using the algorithms presented in this chapter [40, 17, 67]. The energy functions f are chosen based on the model in Equation 2. This forward model only accounts for the attenuation of primary rays and neglects scatter, pile-up, charge sharing and other complex effects, unless those can be taken into account in the effective spectrum.

The following three sections introduce the main classes of spectral CT reconstruction algorithms (see Figure 2): image-based and projection-based, which perform decomposition into materials

and tomographic reconstruction separately, and are therefore referred to as "two-step" methods, and one-step inversion, which merges both decomposition and reconstruction into a single inverse problem. The final sections describe possible regularizers for these ill-posed inverse problems and potential image quality issues specific to spectral CT decomposition and reconstruction.

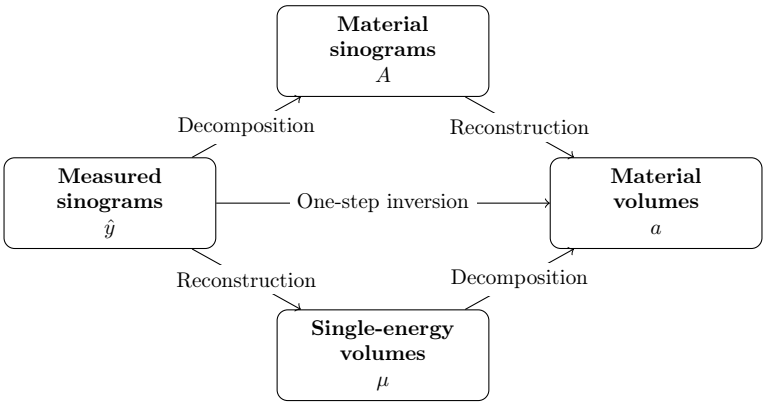

Figure 2: The three classes of inversion methods described in this chapter are image-based decomposition (bottom row, section 1), projection-based decomposition (top row, section 2) and one-step inversion (section 3).

1 Image-based decomposition

Image-based decomposition was initially developed for exploiting two (or more) CT acquisitions obtained at different tube-voltages on a conventional CT scanner [6]. With distinct spectra at different voltages, the resulting CT slices display energy dependent differences. Image-based decomposition assumes that the b-th single-energy CT represents the attenuation coefficient at a given (effective) energy e_b, which is true with mono-energetic CT acquisitions at a synchrotron [79], by reconstructing from the log-transformed projections $\ln(s_b(e_b)/y_{ib})$, or with the use of an efficient beam hardening correction. Under this assumption, the CT image $\mu(\,\cdot\,, e_b)$ of the b-th effective spectrum is, according to Equation 2, a linear combination of the sought space-dependent functions a_m and the energy-dependent functions f_m. Combining the measurements, one obtains at each spatial position $\boldsymbol{x}$ a small linear system of equations with as many equations as CT images:

$$\boldsymbol{\mu}(\boldsymbol{x}) = \boldsymbol{F}\boldsymbol{a}(\boldsymbol{x}) \tag{4}$$

with

$$\boldsymbol{\mu}(\boldsymbol{x}) = \begin{bmatrix} \mu(\boldsymbol{x}, e_1) \\ \mu(\boldsymbol{x}, e_2) \\ \vdots \\ \mu(\boldsymbol{x}, e_\mathrm{B})) \end{bmatrix}, \quad \boldsymbol{F} = \begin{bmatrix} f_1(e_1) & f_2(e_1) & \dots & f_\mathrm{M}(e_1) \\ f_1(e_2) & f_2(e_2) & \dots & f_\mathrm{M}(e_2) \\ \vdots & \vdots & \ddots & \vdots \\ f_1(e_\mathrm{B}) & f_2(e_\mathrm{B}) & \dots & f_\mathrm{M}(e_\mathrm{B}) \end{bmatrix} \quad \text{and} \quad \boldsymbol{a}(\boldsymbol{x}) = \begin{bmatrix} a_1(\boldsymbol{x}) \\ a_2(\boldsymbol{x}) \\ \vdots \\ a_\mathrm{M}(\boldsymbol{x}) \end{bmatrix}. \tag{5}$$

Given its small size, this system can easily be solved, e.g. with the Moore-Penrose pseudo-inverse (which is the inverse of $\boldsymbol{F}$ if $\boldsymbol{F}$ is invertible). Moreover, since there is no spatial dependence of $\boldsymbol{F}$, this (pseudo-)inverse can be computed once for all voxels if the effective energy of the input CT images is known. Otherwise, it can be directly calibrated using materials with known linear attenuation properties. Image-based decomposition can be combined with regularization to e.g. reduce noise [14, 15, 49, 76]. A simulated example using monochromatic spectra is provided in Figure 3.

The simplicity of image-based decomposition makes it an attractive solution. It is also extensively used in applications where access to raw data / sinograms is not available, as demonstrated in radiotherapy applications [80]. Another advantage compared to projection-based inversions is that there is no need to have projections acquired with the same geometry (source and detector positions and orientations) for all effective spectra, as is, for example, the case when two different

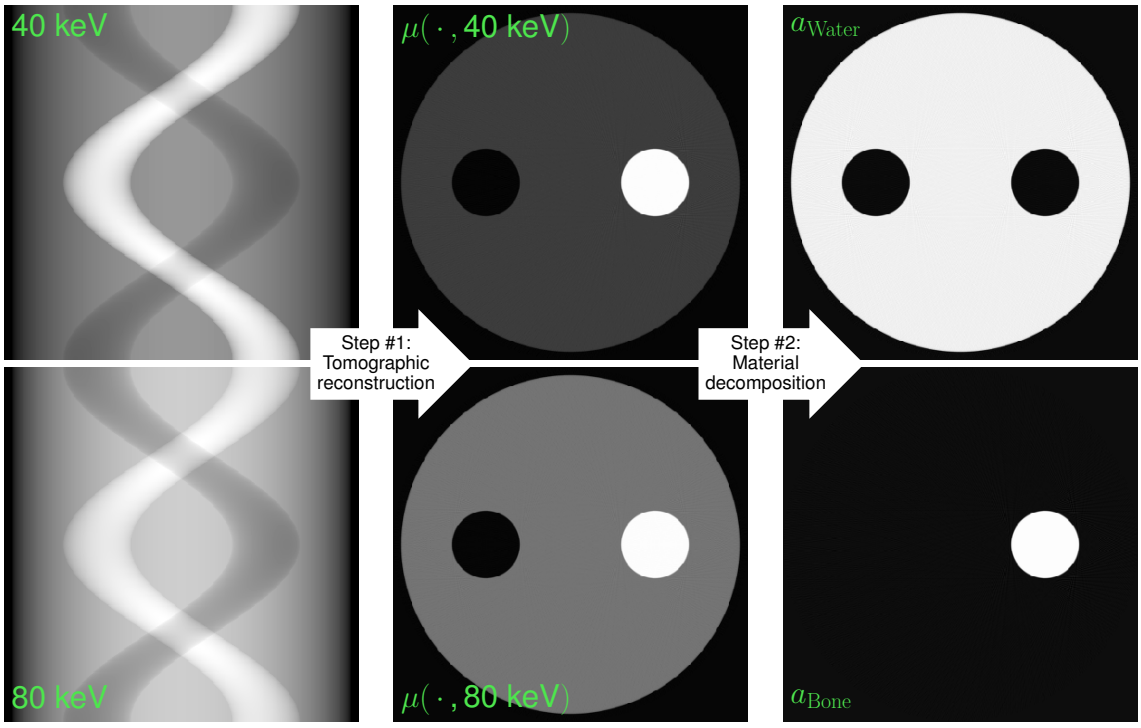

Figure 3: Left: noiseless simulated dual-energy log-transformed sinograms using monochromatic irradiations at 40 keV (top) and 80 keV (bottom). Middle: corresponding single-energy volumes g_b. Right: decomposed volumes a_m. The object is made of a liquid water component (top right) and cortical bone (bottom right). The linear attenuation coefficients used for the simulation are those of ICRP retrieved from x-ray lib [64], i.e., $\mu_{\text{water}}(40\ \text{keV}) = 0.27\,\text{cm}^{-1}$, $\mu_{\text{water}}(80\ \text{keV}) = 0.18\,\text{cm}^{-1}$, $\mu_{\text{water}}(40\ \text{keV}) = 1.19\,\text{cm}^{-1}$ and $\mu_{\text{bone}}(80\ \text{keV}) = 0.41\,\text{cm}^{-1}$.

x-ray sources are used for the acquisition of different spectra. The input CT images must still be perfectly registered, and this is true for all algorithms presented here. Even if two (or more) CT acquisitions could easily be acquired on any clinical CT scanner with different voltages, patient motion, e.g. through breathing, reduces significantly the quality of spectral results. Another significant drawback of image-based decomposition is the impact of beam hardening when using conventional x-ray sources. Inaccuracies of beam hardening correction will have a direct influence on the result [71]. Advanced beam hardening correction algorithms require the knowledge of the linear attenuation coefficients of the materials in the field-of-view, e.g. by relying on the same model as Equation 2 [8]. Image-based decomposition is therefore simple because it forwards the complexity of Equation 3 from the decomposition to the beam hardening correction. The difficulty therefore lies in the latter and has lead to the development of algorithms which correct for beam hardening in the image domain while decomposing by using a different model than Equation 2 [34]. Another approach, intermediate with one-step inversion (section 3), projects the current estimate to iteratively correct for beam hardening [35].

2 Projection-based decomposition

Projection-based methods perform first the decomposition in projection space before reconstructing material specific CT maps (Figure 2).

2.1 Decomposition into material projections

Decomposition into material specific projections aims to determine, for each pixel of the multi-energy sinogram, the corresponding line integral through the spatial maps a_m. For example, if the object consists of two materials as in Figure 3 and the basis functions f_m are the corresponding linear attenuation coefficients of the materials, the aimed decomposed data will be the sinogram of each material, as illustrated in Figure 4. Formally, Equation 3 is modified by inverting the order of the integral over the line $\mathcal{L}_i$ and the discrete sum over the M basis functions. Projection-based decomposition then utilizes the forward model

$$\hat{y}_{ib} = \int_{\mathbb{R}^+} s_b(\epsilon) \exp\left(- \sum_{m=1}^{\mathrm{M}} A_{im} f_m(\epsilon) \right) \mathrm{d}\epsilon \tag{6}$$

with the unknowns $A_{im} = \int_{\mathcal{L}_i} a_m(\boldsymbol{x}) \, \mathrm{d}\ell$ corresponding to the i-th line integral through a_m. This decomposition yields a set $\boldsymbol{A}$ of M sinograms (one per basis function), which can each be reconstructed to obtain one volume per material. Similarly to the image-based problem, decomposing the acquired sinograms $\boldsymbol{y}$ into material specific sinograms $\boldsymbol{A}$ is a small problem when processed pixel-by-pixel, with M unknowns to find from B measurements. However, the exponential function causes the problem to be non-linear and the (weighted) least squares data fidelity term is non-convex [1].

In their seminal paper [4], Alvarez and Macovski proposed to approximate the logarithm of the expectation of the measures $\hat{\boldsymbol{y}}$ by a P-th order polynomial of the A_{im}:

$$\ln \hat{y}_{ib} \simeq \sum_{p_1+p_2+\cdots+p_{\mathrm{M}} \leq \mathrm{P}} \alpha_{p_1 p_2 \ldots p_{\mathrm{M}}} A_{i1}^{p_1} A_{i2}^{p_2} \ldots A_{i\mathrm{M}}^{p_{\mathrm{M}}} \tag{7}$$

with $\{p_1, \ldots, p_{\mathrm{M}}\}$ the exponents and $\alpha_{p_0 p_1 \ldots p_{\mathrm{M}}}$ the coefficients of the polynomial. Another solution is to directly approximate the inversion by a polynomial [28]:

$$A_{im} \simeq \sum_{q_1+q_2+\cdots+q_{\mathrm{B}} \leq \mathrm{P}} \beta_{q_1 q_2 \ldots q_{\mathrm{B}}} \left(\ln \hat{y}_{i1}\right)^{q_1} \left(\ln \hat{y}_{i2}\right)^{q_2} \ldots \left(\ln \hat{y}_{i\mathrm{B}}\right)^{q_{\mathrm{B}}} \tag{8}$$

with $\{q_1, \ldots, q_{\mathrm{B}}\}$ the exponents and $\beta_{q_0 q_1 \ldots q_{\mathrm{B}}}$ the coefficients of this other polynomial. Both methods are very efficient solutions, probably best suited to dual-energy decomposition with two basis functions (B = M = 2). In any case, they are only approximations of Equation 6 or its inverse. The accuracy of this approximation can be improved by increasing the polynomial order P, but it also degrades the stability of the decomposition. Already in [4], the authors did not use all nine possible monomials and later studies suggested a rationale for adequately selecting a subset of monomials [29]. If the effective spectra s are known, the coefficients of the polynomials

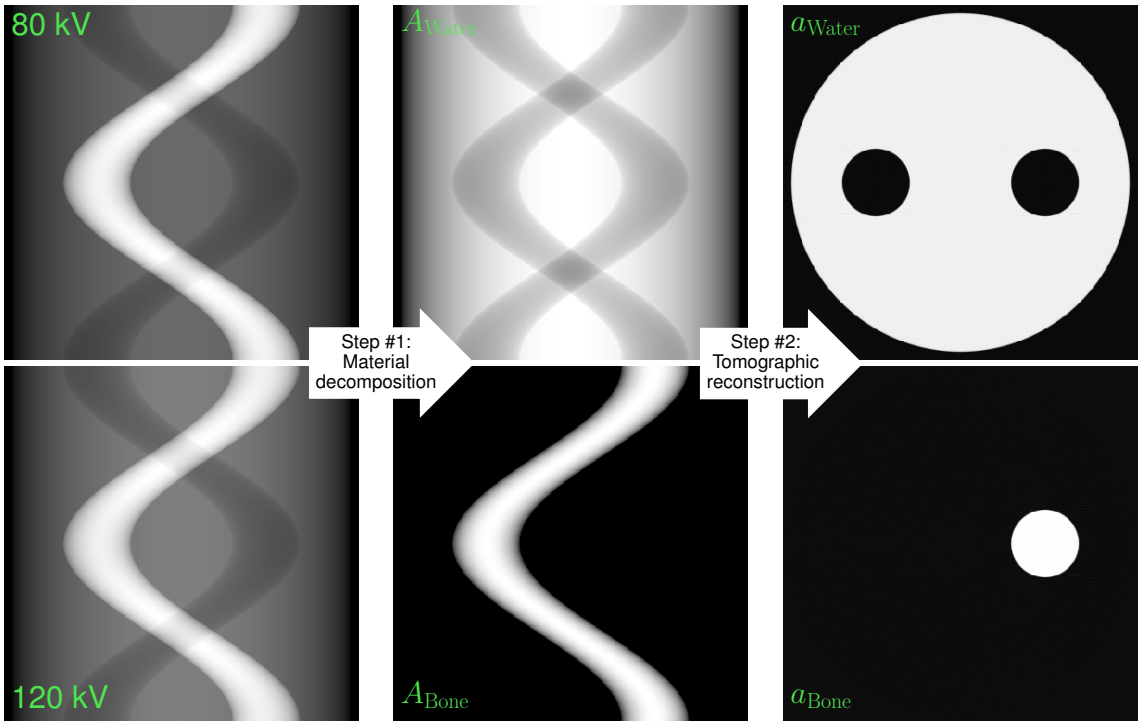

Figure 4: Left: noiseless simulated dual-energy sinograms of the object in Figure 3 using the 80 kV (top) and 120 kV (bottom) spectra and the detector response shown on top of Figure 1. Middle: decomposed sinograms A_m using projection-based decomposition with μ_{water} and μ_{bone} as basis functions f_m. Right: decomposed volumes a_m. The object is the same as in Figure 3.

can be computed to best approximate the forward model, as $\boldsymbol{F}$ in image-based decomposition (Equation 4). Otherwise, one can directly calibrate the polynomial coefficients without estimating s by taking projections through multiple combinations of basis material layers with known thicknesses as, e.g. in the calibration phantom of [2].

In 2008, in order to deal with three materials and four energy bins, Roessl *et al.* proposed to solve the problem in the maximum likelihood sense [57, 62], i.e., to determine which are the most likely A_{im} given the measured y_{ib}. To maximize the log-likelihood, they used the Nelder-Mead downhill simplex method [47], which is a zero order optimization algorithm for convex problems, i.e., which does not need the gradient of the cost function with respect to the optimized variables. Under standard clinical x-ray exposure, the statistical noise on y_{ib} results in very noisy decomposed sinograms, which must be filtered to become usable, as illustrated in Figure 5.

Brendel *et al.* [5] proposed to improve Roessl's optimization using the iterative coordinate descent. They also introduced spatial regularization in their minimization problem to limit noise in decomposed sinograms: in addition to being in agreement with the measured photon counts, the decomposed material line integrals in a pixel i must be similar to those in the neighboring pixels. However, regularizing in the projection domain is unusual and it can negatively impact the reconstructed images if it is inadequately chosen or weighted. Similar approaches based on solving an inverse problem include the work of Ducros *et al.* [16] and Abascal *et al.* [1] solving a weighted least-squares problems using a Gauss-Newton algorithm and an iterative Bregman scheme. The latter authors also used the Kullbac-Leibler divergence [21], which is more adapted to Poisson noise distributions and should lead to a result similar to the maximum likelihood approach of [57, 62].

Intermediate solutions between the polynomial models (Equation 7 and Equation 8) and the full non-linear model (Equation 6) have been tailored for the case of more measurements than basis functions [2, 3, 26, 27, 41, 94]. Another approach is to use machine learning to solve this complex but small problem, e.g. by using a neural network [93].

A significant advantage of projection-based decomposition over image-based decomposition (section 1) is that it does not suffer from beam hardening because the material maps $\boldsymbol{f}$ are energy-independent. However, it can only be applied if the measurements for different spectra are acquired with the same geometry, which is the case for dual-layer detectors and spectral photon counting

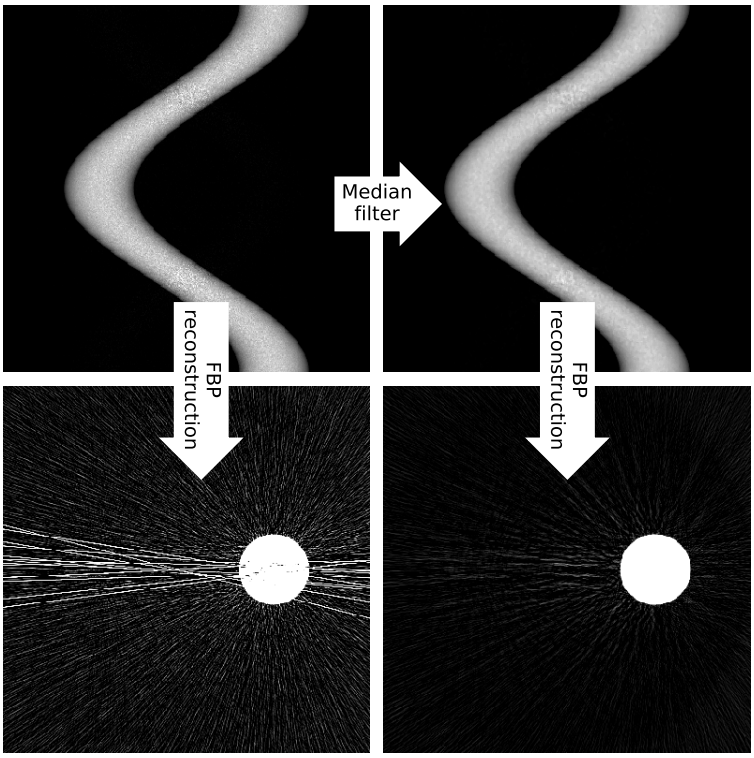

Figure 5: Sinogram of the bone (top) and its reconstruction (bottom) for the same object as Figure 4 with an additional solution of 1 mg/ml gadolinium filling the left hole of the water component. Data simulated using the 5-bin spectral model of the Philips small animal prototype in Lyon [65] corrupted with Poisson noise. The projection-based decomposition is the algorithm of Roessl *et al* [57, 62] with the three-material basis $\boldsymbol{f} = \{\mu_{\text{Water}}, \mu_{\text{Bone}}, \mu_{\text{Gadolinium}}\}$. Images reconstructed with a filtered backprojection reconstruction. The right sinogram resulted from a median filter to remove outliers. Outliers are in the low count area, for rays that traverse both the bone and the gadolinium (see other reconstructions in Figure 6).

detectors but not for dual-source systems or fast-switching x-ray sources. For dual-source or fast-switching systems, one solution is to interpolate the sinograms to have corresponding measurements, but this step could limit the accuracy. Performing several successive acquisitions with different spectra on a standard CT is in theory feasible, but just like with image-based methods, patient motion is then a concern.

2.2 Tomographic reconstruction

None of the methods presented in subsection 2.1 makes any assumption on how the material sinograms are reconstructed once they have been decomposed. In fact, any tomographic reconstruction method can be used, including filtered backprojection algorithms. However, the decomposition is sensitive to noise and it is natural to account for this noise in an iterative reconstruction algorithm. A first solution is to use an estimate of the variance of the decomposed sinograms in a weighted least squares algorithm [61]. The material decomposition process also induces anti-correlated noise between the different materials [22], which suggests the use of reconstruction techniques which also account for covariances [60]. Variances and co-variances can be estimated using the Cramér-Rao lower bound [56]. Sawatzky *et al.* [59] and Mory *et al.* [43] proposed such an approach. The core idea of these methods is that minimizing the usual least-squares data-attachment term yields the Best Linear Unbiased Estimator (BLUE) only when all data samples are uncorrelated and have equal variance. In all other cases, the BLUE is obtained by minimizing a Generalized Least Squares (GLS) term, which involves the inverse of the covariance matrix of the noise. Although GLS is formally simple, it is computationally much more demanding since all material specific CT maps f_m must be reconstructed simultaneously. It is not clear yet whether the improvement in image quality is worth the increased computational complexity [43].

3 One-step inversion

One-step methods generate material maps $\boldsymbol{a}$ straight from recorded photon counts $\boldsymbol{y}$. Similar to projection-based decomposition (section 2), these methods can rely for example on the forward model in Equation 3, but with the advantage of not requiring matching projections (similar to image-based decomposition section 1). It also circumvents the fundamental drawback of all two-step approaches: the first step may introduce errors, which cannot be compensated for in the second step. An excellent illustration of this latter problem is the presence of outliers in sinograms decomposed with non-regularized projection-based methods [57, 62]: as the decomposition process is non-linear, it may strongly amplify the statistical noise on the photon counts, resulting in some pixels with entirely incorrect values for the line integral. Reconstructing without first removing these outliers yields material specific CT maps dominated by powerful streak artifacts (see Figure 5).

3.1 Forward problem and cost function

Most one-step reconstruction methods apply an identical forward model, which is the equivalent to Equation 3 except that the two integrals (over the energies ϵ and the line positions ℓ) are discretized. Note, there is no analytical solution to this problem. Discretizing the line integral is the basis of most iterative single-energy CT reconstruction algorithms and despite being posed as a linear inverse problem, single-energy iterative CT is computationally expensive, which partly explains why manufacturers have only recently started implementing it in commercial CT scanners [50]. One-step spectral CT is even more computationally expensive: with the same number of pixels and voxels, the number of measurements is multiplied by the number B of effective spectra (second index of $\boldsymbol{y}$) and the number of unknowns is multiplied by the number M of basis energy functions (second index of $\boldsymbol{a}$), plus the inverse problem is non-linear.

In the literature, the cost functions are constructed from different terms to solve this problem. For the data-attachment, the most widespread approach is to maximize the likelihood of observing the measurements $\boldsymbol{y}$, given the material specific CT volumes $\boldsymbol{a}$ under the assumption that the measurements are corrupted by Poisson noise [18, 33, 40, 75, 83]. Other methods minimize a weighted-least squares data-attachment term, computed either on the photon counts [77] or on the ratio between photon counts and photon counts if there had been no attenuation [9, 12]. For

the regularization, various conventional options have been considered: positivity [12, 33], total-variation [9, 18], or a similar measure based on the spatial gradient [33, 40, 77, 83].

3.2 Minimization

Given the size and non-linearity of the one-step inversion problem, the primary challenge is to minimize the cost function. Almost every method uses a different algorithm to solve its cost function and the landscape of solutions strongly resembles that of single-energy CT.

Several works attempt to adapt methods developed for single-energy CT which assume a linear problem. Zhao *et al.* [92] linearize the cost function and use an Algebraic Reconstruction Technique (ART) [19]. Li *et al.* [30] do the same using filtered backprojection reconstruction. Cai *et al.* [9] used a non-linear conjugate gradient. Chen *et al.* [12] used a heuristic non-convex adaptation of ASD-POCS [66]. Rodesch *et al.* [54] adapted the maximum likelihood polychromatic algorithm of De Man *et al.* [36].

Several works [33, 40, 83] used separable quadratic surrogates (SQS). The surrogate is a tool for *optimization transfer* [25] which aims at accelerating the minimization of the cost function. Formally, the function $\Phi_{\boldsymbol{x}_0} : \mathbb{R}^N \to \mathbb{R}$ is a surrogate of the cost function $\Psi : \mathbb{R}^N \to \mathbb{R}$ at $\boldsymbol{x}_0 \in \mathbb{R}^N$ if and only if $\Phi_{\boldsymbol{x}_0}$ is above Ψ on $\mathbb{R}^N$, and tangent to Ψ at $\boldsymbol{x}_0$, i.e.,

$$\left\{\begin{array}{lcll} \Phi_{\boldsymbol{x}_0}(\boldsymbol{x}) & \geq & \Psi(\boldsymbol{x}) & \forall \boldsymbol{x} \in \mathbb{R}^N, \\ \Phi_{\boldsymbol{x}_0}(\boldsymbol{x}_0) & = & \Psi(\boldsymbol{x}_0) & \text{and} \\ \Phi'_{\boldsymbol{x}_0}(\boldsymbol{x}_0) & = & \Psi'(\boldsymbol{x}_0). & \end{array}\right. \tag{9}$$

It is separable if the contribution to Φ of one or a few unknowns can be separated from the ones of the other unknowns. The advantage is that the minimization can be split into many sub-problems, each with one or a few unknowns, which can be solved in one iteration of Newton's algorithm if these sub-problems are quadratic. For spectral CT reconstruction, the existing SQS allows solving a sub-problem with M unknowns per pixel [33, 40, 83]. Two SQS have been derived in the literature for one step reconstruction [33, 83], but the inequality in Equation 9 is only demonstrated for the one in [33]. Since the problem is non-convex, SQS minimization would retrieve a local minimum if the initialization is not adequately chosen [33].

Some algorithms address the non-convexity using a primal-dual metric algorithm. Foygel Barber *et al* developed the *Mirrored Convex/Concave Optimization for Nonconvex Composite Functions* (MOCCA) [18, 63], a primal-dual scheme derived from the Chambolle-Pock algorithm [11]. Tairi *et al* [75] used a variable-metric primal algorithm [13].

Several of these algorithms have been compared in [44] on a simulated test case (three-material decomposition from a 5-bin photon counting detector). All the algorithms converged to a visually similar solution, but there were substantial differences in convergence speed. Figure 6 demonstrates the potential benefit of one-step reconstruction, but it is clear that further research is required before one-step reconstruction can be routinely applied in a spectral CT scanner.

4 Regularization

The problem of decomposition and reconstruction for spectral CT is an ill-posed inverse problem, as is tomographic reconstruction alone [46]. Regularization is therefore required to obtain satisfying results.

In two-step decomposition algorithms, the regularization may be applied to each of the two steps, as pointed out in section 1 and section 2. Regularizing the first step is probably mandatory in both cases: this is well-known for tomographic CT reconstruction, the first step of image-based methods, and it empirically seems to be the case in projection-based decomposition (Figure 5), although this may depend on the number M of basis functions and the number B of effective spectra. The choice of the regularization and its strength is sensitive because it will impact the inputs of the second step. Inverting the decomposition in one step alleviates this difficulty.

There are many options for the regularization of spectral CT. As pointed out in section 2, only a small number of studies have suggested to regularize the decomposition of projections [1, 5, 16]. In general, the regularization is rather applied to the CT maps, i.e. in the image domain. Any regularization used in tomographic reconstruction may be applied to each volume independently, e.g. total variation (TV) [18, 63] or a differentiable approximation of TV [33, 40, 78, 83] (Figure 7),

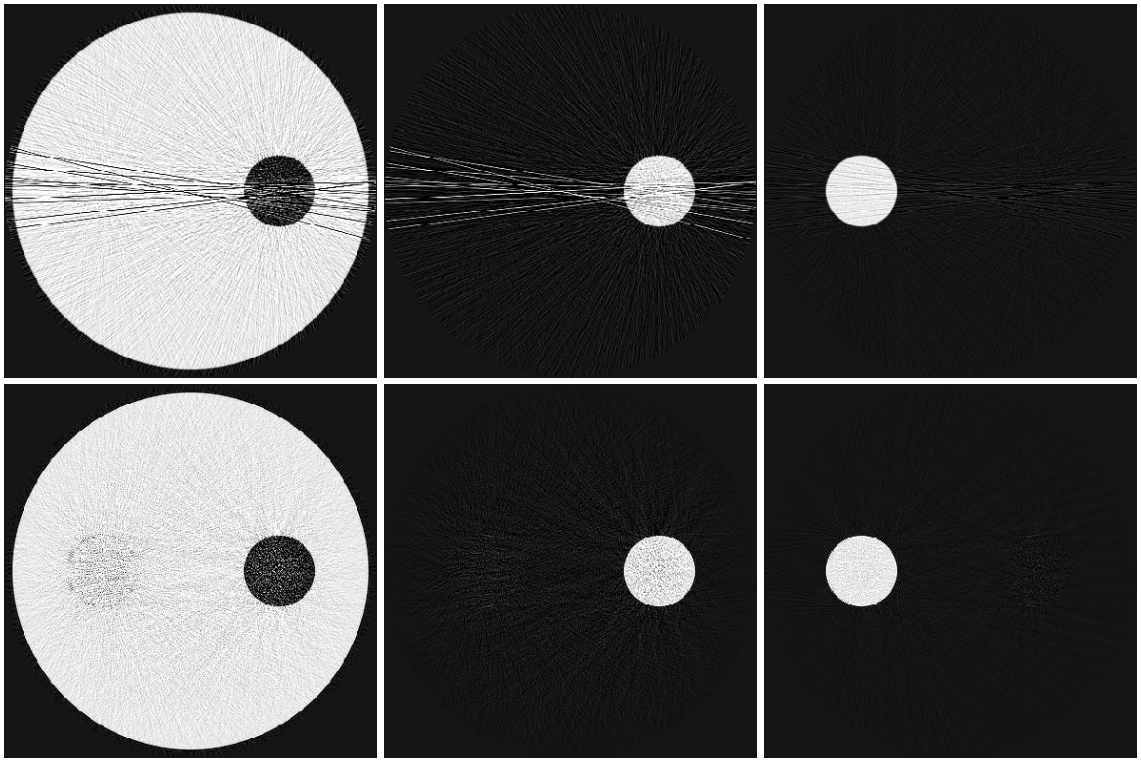

Figure 6: Projection-based (top, algorithm of [57, 62] combined with filtered-backprojection reconstruction) and one-step reconstruction (bottom, 500 iterations of the algorithm of [40] without subsets and without regularization) using the spectral model and the object described in Figure 5. From left to right: water, bone and gadolinium maps. The gray scale is $\pm 10\%$ around the target concentration of each material.

the $\ell 1$-norm of wavelets coefficients [87] or the $\ell 0$-norm of dictionaries [91]. Several such regularizers have been compared for spectral CT in [58].

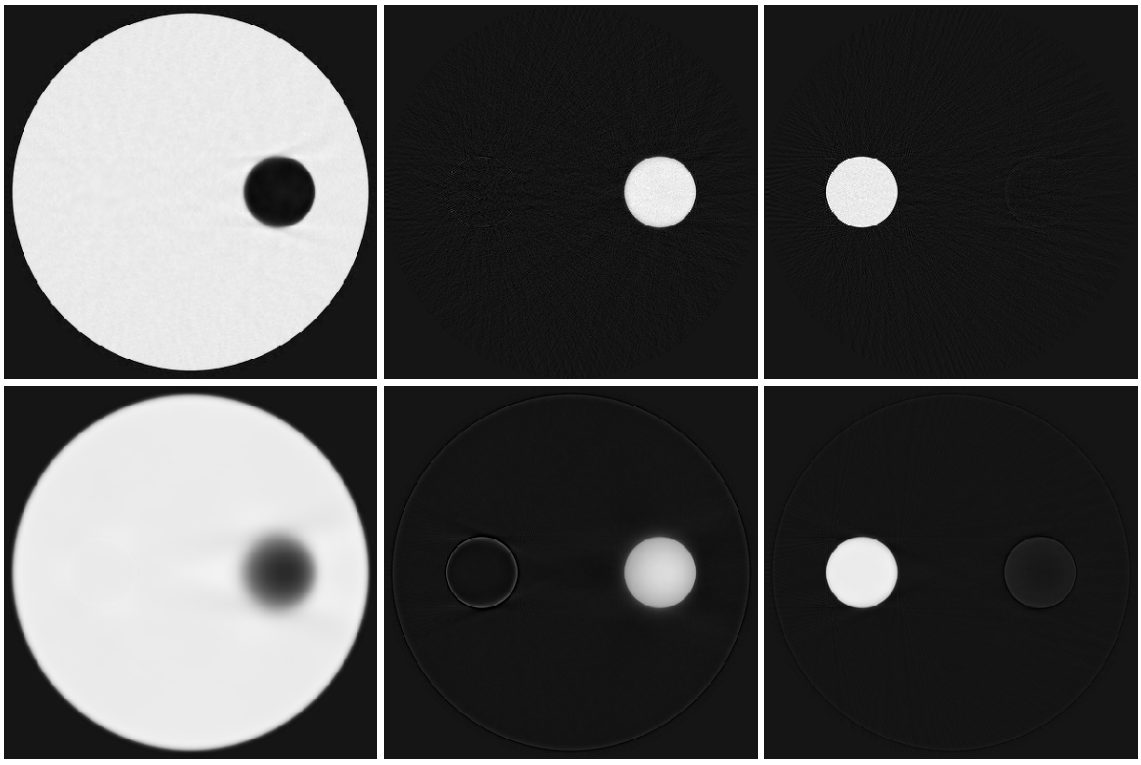

Figure 7: Effect of regularization on one-step reconstruction [40] from the same data as in Figure 6. The regularizer is Green's approximation of TV [20] on each material specfic CT map. The number of iterations was increased to 1000 to reach (visual) convergence. The regularization weights (one-per material specific CT map) have been first chosen to be maximum without visible cross-talk (top) and 100 times larger each (bottom). The grayscale is the same as in Figure 6.

Some authors have suggested to assume that the material specific CT maps share the same structures and developed regularizations to take advantage of this similarity to improve the results. Similar strategies have been developed for dual-modality imaging such as anatomical priors from CT used in positron emission tomography (PET) reconstruction [52]. Total nuclear variation is a generalization of total variation to multi-channel images, which was proposed for this specific goal [53]. Like TV, it favors a piecewise constant volume for each material, but it also favors volumes where edges have the same location and orientation. Several other multi-channel regularizers have been applied to spectral CT data [24, 48, 86].

A final class of regularization is the use of constraints to overcome a larger number of material specific CT maps than energy measurements ($M > B$) [31, 32, 33, 42, 89]. Additional constraints are added to those in Equation 4 or Equation 6 by assuming some pre-defined properties of the scanned materials based on volume and/or mass preservation between the sum of each material specific CT maps and the mixture. These techniques have been applied in all types of inversions, image-based [32, 42, 31], projection-based [89] and one-step [33].

5 Image quality issues specific to spectral CT

Spectral CT scanners can reconstruct regular CT-like volumes: the photon counts obtained from a spectral CT acquisition can be either fed to one of the spectral CT reconstruction methods described above, yielding material specific maps, or merged back together into a single sinogram and reconstructed, generating a regular-CT volume (e.g. in Hounsfield Units, HU). Although they are reconstructed from identical input data, it turns out that material specific CT volumes are typically much noisier than their HU counterpart. The two fundamental reasons for this phenomenon are: reconstructing several volumes instead of a single one reduces the amount of measured photons

used per voxel, which results in higher noise (which can be compensated for by increasing the radiation exposure), and the non-linear decomposition process amplifies the noise.

With the introduction of photon-counting detectors into clinical routine, one can expect to see a reduction in detector pixel sizes [69, 84]. The increase in spatial resolution will extend the diagnostic range of CT imaging, for example in the visualization of fine structures in the lung or along coronary arteries with stents [37, 65, 68]. In those cases, the high-resolution acquisition enables an improved sampling of high-frequency features and reduces noise aliasing [51]. However, for sections without fine details, a high-frequency noise will significantly reduce the image quality. In the future, it will be essential to incorporate these new circumstances into the image reconstruction and to optimize it through algorithmic solutions still to be developed. On this note, the additional energy dimension provides an increased amount of information, which can be utilized to de-noise spectral images. The data can be utilized following strategies like prior image constraints [90] or dictionaries [39, 85] (section 4).

Additionally, material volumes are subject to decomposition errors, commonly referred to as "cross-talk": materials can appear in the wrong material specific CT volumes. The severity of cross-talk depends on how much the materials' attenuation profiles differ from each other (the more similar they are, the stronger the cross-talk) and on how much noise is present in the photon counts (the noisier the data, the stronger the cross-talk). In one-step inversion methods, regularization can also cause cross-talk: regularizing one material creates discrepancies between the estimated photon counts and the measured ones, which are compensated by adding or removing some amount of another material. This effect is particularly intense on the borders of structures when a strong spatial regularization is applied, as illustrated in Figure 7.

Ring artifacts are a very common artifact in any type of CT imaging and can have a variety of sources. In conventional CT, if one detector element is out of calibration, the reading of this element may consistently be incorrect. As a consequence, the later reconstructed CT slice will be affected by rings. As photon-counting detectors are highly complex and sensitive compared to conventional detectors, a dedicated calibration needs to be performed. While this spectral technology, as well as calibration methods, are still under development, rings that may appear after reconstruction can be removed to a large degree by classical ring removal algorithms [45, 88]. Regarding rings or other artifacts, it is essential to understand that the current hardware does not represent an ideal detector. Novel sensor material (imperative for photon-counting CT), along the lines of cadmium telluride and cadmium zinc telluride, come with technical challenges which can be addressed by hardware as well as software solutions. Pile-up and spectral distortions are two of the main effects which reduce the quality of spectral data from photon-counting detectors. Several investigators have developed techniques to model those shortcomings with different software-based techniques [10, 55, 70, 74, 72, 73]. These achievements represent an ideal opportunity to overcome some of those hardware shortcomings but they still need to be integrated in the image formation algorithms described in this chapter.

6 Conclusion

Spectral CT systems, especially systems equipped with a spectral photon-counting detector, are a promising development for the clinical routine. Many benefits concerning the diagnostic range have been discussed, which include low-dose, high-resolution, quantitative and K-edge imaging. First prototype systems [69, 84] have been installed and have demonstrated benefits along the same lines. At the same time, one has to realize that this development comes with challenges which translate into non-ideal imaging performances. The harmonization between hardware and software will significantly aid the process of overcoming those current shortcomings. In this chapter, we presented algorithmic solutions which address a wide range of possible spectral CT implementations and the challenges which come along with each of them. In three sections, we introduced the main classes of spectral CT reconstruction algorithms: image-based and projection-based, which perform decomposition into materials and tomographic reconstruction separately and are therefore referred to as "two-step" methods, and one-step inversion, which merges both decomposition and reconstruction into a single inverse problem. For the coming years, while spectral CT will fully translate into the clinical routine, further algorithmic developments will be necessary to improve, for example, the sensitivity, to constantly extend the diagnostic range of CT imaging.

References

[1] J.F.P.J. Abascal, N. Ducros, and F. Peyrin. Nonlinear material decomposition using a regularized iterative scheme based on the Bregman distance. 34:124003, 2018.

[2] R.E. Alvarez. Estimator for photon counting energy selective x-ray imaging with multibin pulse height analysis. *Med Phys*, 38(5):2324–2334, May 2011.

[3] R.E. Alvarez. Efficient, non-iterative estimator for imaging contrast agents with spectral x-ray detectors. *IEEE Transactions on Medical Imaging*, 35(4):1138–1146, April 2016.

[4] R.E. Alvarez and A. Macovski. Energy-selective reconstructions in X-ray computerized tomography. *Phys Med Biol*, 21(5):733–744, Sep 1976.

[5] B. Brendel, F. Bergner, K. Brown, and T. Koehler. Penalized likelihood decomposition for dual layer spectral CT. In *Fourth international conference on image formation in X-ray computed tomography*, Bamberg, Germany, 2016.

[6] R.A. Brooks. A quantitative theory of the hounsfield unit and its application to dual energy scanning. *J Comput Assist Tomogr*, 1(4):487–493, Oct 1977.

[7] R.A. Brooks and G. Di Chiro. Beam hardening in x-ray reconstructive tomography. *Phys Med Biol*, 21(3):390–398, May 1976.

[8] T.M. Buzug. *Computed tomography: from photon statistics to modern cone-beam CT*. Springer Science & Business Media, 2008.

[9] C. Cai, T. Rodet, S. Legoupil, and A. Mohammad-Djafari. A full-spectral bayesian reconstruction approach based on the material decomposition model applied in dual-energy computed tomography. *Medical physics*, 40:111916, November 2013.

[10] J. Cammin, J. Xu, W.C. Barber, J.S. Iwanczyk, N.E. Hartsough, and K. Taguchi. A cascaded model of spectral distortions due to spectral response effects and pulse pileup effects in a photon-counting x-ray detector for CT. *Medical physics*, 41(4):041905, 2014.

[11] A. Chambolle and T. Pock. A first-order primal-dual algorithm for convex problems with applications to imaging. *Journal of Mathematical Imaging and Vision*, 40(1):120–145, 2011.

[12] B. Chen, Z. Zhang, E.Y. Sidky, D. Xia, and X. Pan. Image reconstruction and scan configurations enabled by optimization-based algorithms in multispectral CT. *Physics in medicine and biology*, 62:8763–8793, November 2017.

[13] E. Chouzenoux, J.-C. Pesquet, and A. Repetti. Variable metric forward–backward algorithm for minimizing the sum of a differentiable function and a convex function. *Journal of Optimization Theory and Applications*, 162(1):107–132, 2014.

[14] Q. Ding, T. Niu, X. Zhang, and Y. Long. Image-domain multi-material decomposition for dual-energy CT based on prior information of material images. *Medical physics*, May 2018.

[15] X. Dong, T. Niu, and L. Zhu. Combined iterative reconstruction and image-domain decomposition for dual energy CT using total-variation regularization. *Medical Physics*, 41(5):051909, 2014.

[16] N. Ducros, J.F.P.-J. Abascal, B. Sixou, S. Rit, and F. Peyrin. Regularization of nonlinear decomposition of spectral x-ray projection images. *Medical physics*, 44:e174–e187, September 2017.

[17] S. Ehn, T. Sellerer, K. Mechlem, A. Fehringer, M. Epple, J. Herzen, F. Pfeiffer, and P.B. Noël. Basis material decomposition in spectral CT using a semi-empirical, polychromatic adaption of the Beer-Lambert model. *Physics in medicine and biology*, 62:N1–N17, January 2017.

[18] R. Foygel Barber, E.Y. Sidky, T. Gilat Schmidt, and X. Pan. An algorithm for constrained one-step inversion of spectral CT data. *Phys Med Biol*, 61(10):3784–3818, May 2016.

[19] R. Gordon, R. Bender, and G.T. Herman. Algebraic reconstruction techniques (ART) for three-dimensional electron microscopy and X-ray photography. *Journal of Theroretical Biology*, 29(3):471–481, Dec 1970.

[20] P.J. Green. Bayesian reconstructions from emission tomography data using a modified EM algorithm. *IEEE Transactions on Medical Imaging*, 9(1):84–93, 1990.

[21] T. Hohweiller, N. Ducros, F. Peyrin, and B. Sixou. Spectral CT material decomposition in the presence of Poisson noise: a Kullback–Leibler approach. *IRBM*, 38(4):214–218, 2017. Research in Imaging and Health TechnologieS 2017 (RITS 2017).

[22] W.A. Kalender, E. Klotz, and L. Kostaridou. An algorithm for noise suppression in dual energy CT material density images. *IEEE Transactions on Medical Imaging*, 7(3):218–224, September 1988.

[23] W.A. Kalender, W.H. Perman, J.R. Vetter, and E. Klotz. Evaluation of a prototype dual-energy computed tomographic apparatus. I. Phantom studies. *Medical physics*, 13:334–339, 1986.

[24] D. Kazantsev, J.S. Jørgensen, M.S. Andersen, W.R.B. Lionheart, P.D. Lee, and P.J. Withers. Joint image reconstruction method with correlative multi-channel prior for x-ray spectral computed tomography. *Inverse Problems*, 34(6):064001, 2018.

[25] K. Lange, D.R. Hunter, and I. Yang. Optimization transfer using surrogate objective functions. *Journal of Computational and Graphical Statistics*, 9(1):1–20, 2000.

[26] O. Lee, S. Kappler, C. Polster, and K. Taguchi. Estimation of basis line-integrals in a spectral distortion-modeled photon counting detector using low-order polynomial approximation of x-ray transmittance. *IEEE Transactions on Medical Imaging*, 36(2):560–573, February 2017.

[27] O. Lee, S. Kappler, C. Polster, and K. Taguchi. Estimation of basis line-integrals in a spectral distortion-modeled photon counting detector using low-rank approximation-based x-ray transmittance modeling: K-edge imaging application. *IEEE Transactions on Medical Imaging*, 36(11):2389–2403, November 2017.

[28] L.A. Lehmann, R.E. Alvarez, A. Macovski, W.R. Brody, N.J. Pelc, S.J. Riederer, and A.L. Hall. Generalized image combinations in dual KVP digital radiography. *Med Phys*, 8(5):659–667, 1981.

[29] J.-M. Letang, N. Freud, and G. Peix. Signal-to-noise ratio criterion for the optimization of dual-energy acquisition using virtual x-ray imaging: application to glass wool. *Journal of Electronic Imaging*, 13(3):436–449, 2004.

[30] M. Li, Y. Zhao, and P. Zhang. Accurate iterative FBP reconstruction method for material decomposition of dual energy CT. *IEEE Transactions on Medical Imaging*, 2018.

[31] Z. Li, S. Leng, L. Yu, Z. Yu, and C.H. McCollough. Image-based material decomposition with a general volume constraint for photon-counting CT. *Proceedings of SPIE–the International Society for Optical Engineering*, 9412, 2015.

[32] X. Liu, L. Yu, A.N. Primak, and C.H. McCollough. Quantitative imaging of element composition and mass fraction using dual-energy CT: three-material decomposition. *Medical physics*, 36:1602–1609, May 2009.

[33] Y. Long and J.A. Fessler. Multi-material decomposition using statistical image reconstruction for spectral CT. 33(8):1614–1626, 2014.

[34] C. Maass, M. Baer, and M. Kachelriess. Image-based dual energy CT using optimized precorrection functions: a practical new approach of material decomposition in image domain. *Medical physics*, 36:3818–3829, August 2009.

[35] C. Maass, E. Meyer, and M. Kachelriess. Exact dual energy material decomposition from inconsistent rays (MDIR). *Medical physics*, 38:691–700, February 2011.

[36] B. De Man, J. Nuyts, P. Dupont, G. Marchal, and P. Suetens. An iterative maximum-likelihood polychromatic algorithm for CT. *IEEE transactions on medical imaging*, 20:999–1008, October 2001.

[37] M. Mannil, T. Hickethier, J. von Spiczak, M. Baer, A. Henning, M. Hertel, B. Schmidt, T. Flohr, D. Maintz, and H. Alkadhi. Photon-counting CT: high-resolution imaging of coronary stents. *Investigative radiology*, 53:143–149, March 2018.

[38] C.H. McCollough, S. Leng, L. Yu, and J.G. Fletcher. Dual- and multi-energy CT: Principles, technical approaches, and clinical applications. *Radiology*, 276(3):637–653, Sep 2015.

[39] K. Mechlem, S. Allner, S. Ehn, K. Mei, E. Braig, D. Münzel, F. Pfeiffer, and P.B. Noël. A post-processing algorithm for spectral CT material selective images using learned dictionaries. *Biomedical Physics & Engineering Express*, 3(2):025009, 2017.

[40] K. Mechlem, S. Ehn, T. Sellerer, E. Braig, D. Münzel, F. Pfeiffer, and P.B. Noël. Joint statistical iterative material image reconstruction for spectral computed tomography using a semi-empirical forward model. *IEEE transactions on medical imaging*, 37:68–80, January 2018.

[41] K. Mechlem, T. Sellerer, S. Ehn, D. Münzel, E. Braig, J. Herzen, P. B. Noël, and F. Pfeiffer. Spectral angiography material decomposition using an empirical forward model and a dictionary-based regularization. *IEEE Transactions on Medical Imaging*, page 1, 2018.

[42] P. Mendonca, P. Lamb, and D. Sahani. A flexible method for multi-material decomposition of dual-energy CT images. *IEEE Trans Med Imaging*, 33(1):99–116, 2014.

[43] C. Mory, B. Brendel, K. Erhard, and S. Rit. Generalized least squares for spectral and dual energy CT: a simulation study. In *Sixth international conference on image formation in X-ray computed tomography*, pages 98–101, Salt Lake City, USA, 2018.

[44] C. Mory, B. Sixou, S. Si-Mohamed, L. Boussel, and S. Rit. Comparison of five one-step reconstruction algorithms for spectral CT. *Physics in Medicine and Biology*, 2018.

[45] B. Münch, P. Trtik, F. Marone, and M. Stampanoni. Stripe and ring artifact removal with combined wavelet–Fourier filtering. *Optics express*, 17:8567–8591, May 2009.

[46] F. Natterer. *The mathematics of computerized tomography*. John Wiley & Sons, 1986.

[47] J.A. Nelder and R. Mead. A simplex method for function minimization. *The Computer Journal*, 7(4):308–313, 1965.

[48] S. Niu, G. Yu, J. Ma, and J. Wang. Nonlocal low-rank and sparse matrix decomposition for spectral CT reconstruction. *Inverse problems*, 34, February 2018.

[49] T. Niu, X. Dong, M. Petrongolo, and L. Zhu. Iterative image-domain decomposition for dual-energy CT. *Med Phys*, 41(4):041901, Apr 2014.

[50] X. Pan, E.Y. Sidky, and M. Vannier. Why do commercial CT scanners still employ traditional, filtered back-projection for image reconstruction? *Inverse problems*, 25:1230009, January 2009.

[51] A. Pourmorteza, R. Symons, A. Henning, S. Ulzheimer, and D.A. Bluemke. Dose efficiency of quarter-millimeter photon-counting computed tomography: first-in-human results. *Investigative radiology*, 53:365–372, June 2018.

[52] J. Qi and R.M. Leahy. Iterative reconstruction techniques in emission computed tomography. *Physics in medicine and biology*, 51:R541–R578, August 2006.

[53] D.S. Rigie and P.J. La Rivière. Joint reconstruction of multi-channel, spectral ct data via constrained total nuclear variation minimization. *Phys Med Biol*, 60(5):1741–1762, Feb 2015.

[54] P.-A. Rodesch, V. Rebuffel, C. Fournier, F. Forbes, and L. Verger. Spectral CT reconstruction with an explicit photon-counting detector model: a one-step approach. In *Medical Imaging 2018: Physics of Medical Imaging*, volume 10573, page 1057353. International Society for Optics and Photonics, 2018.

[55] E. Roessl, H. Daerr, and R. Proksa. A fourier approach to pulse pile-up in photon-counting x-ray detectors. *Medical physics*, 43:1295–1298, March 2016.

[56] E. Roessl and C. Herrmann. Cramér-Rao lower bound of basis image noise in multiple-energy x-ray imaging. *Physics in medicine and biology*, 54:1307–1318, March 2009.

[57] E. Roessl and R. Proksa. K-edge imaging in x-ray computed tomography using multi-bin photon counting detectors. *Phys Med Biol*, 52(15):4679–4696, Aug 2007.

[58] M. Salehjahromi, Y. Zhang, and H. Yu. Comparison study of regularizations in spectral computed tomography reconstruction. *Sensing and Imaging*, 19, 2018.

[59] A. Sawatzky, Q. Xu, C.O. Schirra, and M.A. Anastasio. Proximal ADMM for multi-channel image reconstruction in spectral x-ray CT. 33(8):1657–1668, 2014.

[60] C.O. Schirra, B. Brendel, M.A. Anastasio, and E. Roessl. Spectral CT: a technology primer for contrast agent development. *Contrast Media Mol Imaging*, 9(1):62–70, 2014.

[61] C.O. Schirra, E. Roessl, T. Koehler, B. Brendel, A. Thran, D. Pan, M.A. Anastasio, and R. Proksa. Statistical reconstruction of material decomposed data in spectral CT. 32(7):1249–1257, 2013.

[62] J.P. Schlomka, E. Roessl, R. Dorscheid, S. Dill, G. Martens, T. Istel, C. Bäumer, C. Herrmann, R. Steadman, G. Zeitler, A. Livne, and R. Proksa. Experimental feasibility of multi-energy photon-counting K-edge imaging in pre-clinical computed tomography. *Phys Med Biol*, 53(15):4031–4047, Aug 2008.

[63] T. Schmidt, R. Barber, and E. Sidky. A spectral CT method to directly estimate basis material maps from experimental photon-counting data. *IEEE transactions on medical imaging*, April 2017.

[64] T. Schoonjans, A. Brunetti, B. Golosio, M. Sanchez del Rio, V.A. Solé, C. Ferrero, and L. Vincze. The xraylib library for X-ray–matter interactions. recent developments. *Spectrochimica Acta Part B: Atomic Spectroscopy*, 66(11-12):776–784, nov 2011.

[65] S. Si-Mohamed, D. Bar-Ness, M. Sigovan, D.P. Cormode, P. Coulon, E. Coche, A. Vlassenbroek, G. Normand, L. Boussel, and P. Douek. Review of an initial experience with an experimental spectral photon-counting computed tomography system. *Nuclear Instruments and Methods in Physics Research Section A: Accelerators, Spectrometers, Detectors and Associated Equipment*, 2017.

[66] E.Y. Sidky and X. Pan. Image reconstruction in circular cone-beam computed tomography by constrained, total-variation minimization. *Phys Med Biol*, 53(17):4777–4807, Sep 2008.

[67] E.Y. Sidky, L. Yu, X. Pan, Y. Zou, and M. Vannier. A robust method of x-ray source spectrum estimation from transmission measurements: Demonstrated on computer simulated, scatter-free transmission data. *Journal of applied physics*, 97(12):124701, 2005.

[68] R. Symons, Y. De Bruecker, J. Roosen, L. Van Camp, T.E. Cork, S. Kappler, S. Ulzheimer, V. Sandfort, D.A. Bluemke, and A. Pourmorteza. Quarter-millimeter spectral coronary stent imaging with photon-counting CT: Initial experience. *Journal of Cardiovascular Computed Tomography*, 2018.

[69] K. Taguchi. Energy-sensitive photon counting detector-based X-ray computed tomography. *Radiological physics and technology*, 10:8–22, March 2017.

[70] K. Taguchi, E.C. Frey, X. Wang, J.S. Iwanczyk, and W.C. Barber. An analytical model of the effects of pulse pileup on the energy spectrum recorded by energy resolved photon counting x-ray detectors. *Medical physics*, 37:3957–3969, August 2010.

[71] K. Taguchi, T. Itoh, M.K. Fuld, E. Fournie, O. Lee, and K. Noguchi. "X-Map 2.0" for edema signal enhancement for acute ischemic stroke using non-contrast-enhanced dual-energy computed tomography. *Investigative radiology*, 53:432–439, July 2018.

[72] K. Taguchi, C. Polster, O. Lee, K. Stierstorfer, and S. Kappler. Spatio-energetic cross talk in photon counting detectors: detector model and correlated Poisson data generator. *Medical physics*, 43:6386, December 2016.

[73] K. Taguchi, K. Stierstorfer, C. Polster, O. Lee, and S. Kappler. Spatio-energetic cross-talk in photon counting detectors: numerical detector model (PcTK) and workflow for CT image quality assessment. *Medical physics*, 45:1985–1998, May 2018.

[74] K. Taguchi, M. Zhang, E.C. Frey, X. Wang, J.S. Iwanczyk, E. Nygard, N.E. Hartsough, B.M.W. Tsui, and W.C. Barber. Modeling the performance of a photon counting x-ray detector for CT: energy response and pulse pileup effects. *Medical physics*, 38:1089–1102, February 2011.

[75] S. Tairi, S. Anthoine, C. Morel, and Y. Boursier. Simultaneous reconstruction and separation in a spectral CT framework with a proximal variable metric algorithm. In *Sixth international conference on image formation in X-ray computed tomography*, Salt Lake City, USA, 2018.

[76] S. Tao, K. Rajendran, C.H. McCollough, and S. Leng. Material decomposition with prior knowledge aware iterative denoising (MD-PKAID). *Physics in medicine and biology*, August 2018.

[77] S. Tilley, M. Jacobson, Q. Cao, M. Brehler, A. Sisniega, W. Zbijewski, and J.W. Stayman. Penalized-likelihood reconstruction with high-fidelity measurement models for high-resolution cone-beam imaging. *IEEE Transactions on Medical Imaging*, 37(4):988–999, April 2018.

[78] S. Tilley, W. Zbijewski, J.H. Siewerdsen, and J.W. Stayman. A general CT reconstruction algorithm for model-based material decomposition. *Proceedings of SPIE–the International Society for Optical Engineering*, 10573, March 2018.

[79] M. Torikoshi, T. Tsunoo, M. Sasaki, M. Endo, Y. Noda, Y. Ohno, T. Kohno, K. Hyodo, K. Uesugi, and N. Yagi. Electron density measurement with dual-energy x-ray CT using synchrotron radiation. *Phys Med Biol*, 48(5):673–685, Mar 2003.

[80] W. van Elmpt, G. Landry, M. Das, and F. Verhaegen. Dual energy CT in radiotherapy: Current applications and future outlook. *Radiother Oncol*, 119(1):137–144, Apr 2016.

[81] G. Vilches-Freixas, J.M. Létang, S. Brousmiche, E. Romero, M. Vila Oliva, D. Kellner, H. Deutschmann, P. Keuschnigg, P. Steininger, and S. Rit. Technical note: Procedure for the calibration and validation of kilo-voltage cone-beam CT models. *Medical Physics*, 43(9):5199–5204, 2016.

[82] X. Wang, D. Meier, K. Taguchi, D.J. Wagenaar, B.E. Patt, and E.C. Frey. Material separation in x-ray CT with energy resolved photon-counting detectors. *Medical physics*, 38:1534–1546, March 2011.

[83] T. Weidinger, T.M. Buzug, T. Flohr, S. Kappler, and K. Stierstorfer. Polychromatic iterative statistical material image reconstruction for photon-counting computed tomography. *Int J Biomed Imaging*, 2016:5871604, 2016.

[84] M.J. Willemink, M. Persson, A. Pourmorteza, N.J. Pelc, and D. Fleischmann. Photon-counting CT: technical principles and clinical prospects. *Radiology*, 289:293–312, November 2018.

[85] W. Wu, Y. Zhang, Q. Wang, F. Liu, P. Chen, and H. Yu. Low-dose spectral CT reconstruction using image gradient $\ell 0$–norm and tensor dictionary. *Applied Mathematical Modelling*, 63:538–557, 2018.

[86] W. Wu, Y. Zhang, Q. Wang, F. Liu, F. Luo, and H. Yu. Spatial-spectral cube matching frame for spectral CT reconstruction. *Inverse Problems*, 34(10):104003, 2018.

[87] Q. Xu, A. Sawatzky, M.A. Anastasio, and C.O. Schirra. Sparsity-regularized image reconstruction of decomposed K-edge data in spectral CT. *Phys Med Biol*, 59(10):N65–N79, May 2014.

[88] L. Yan, T. Wu, S. Zhong, and Q. Zhang. A variation-based ring artifact correction method with sparse constraint for flat-detector CT. *Phys Med Biol*, 61(3):1278–1292, Feb 2016.

[89] L. Yu, X. Liu, and C.H. McCollough. Pre-reconstruction three-material decomposition in dual-energy CT. In *Medical Imaging 2009: Physics of Medical Imaging*, volume 7258, page 72583V. International Society for Optics and Photonics, 2009.

[90] Z. Yu, S. Leng, Z. Li, and C.H. McCollough. Spectral prior image constrained compressed sensing (spectral PICCS) for photon-counting computed tomography. *Physics in medicine and biology*, 61:6707–6732, September 2016.

[91] B. Zhao, H. Ding, Y. Lu, G. Wang, J. Zhao, and S. Molloi. Dual-dictionary learning-based iterative image reconstruction for spectral computed tomography application. *Physics in medicine and biology*, 57:8217–8229, December 2012.

[92] Y. Zhao, X. Zhao, and P. Zhang. An extended algebraic reconstruction technique (e-art) for dual spectral CT. 34(3):761–768, 2015.

[93] K.C. Zimmerman and T.G. Schmidt. Experimental comparison of empirical material decomposition methods for spectral CT. *Phys Med Biol*, 60(8):3175–3191, Apr 2015.

[94] Y. Zou and M.D. Silver. Analysis of fast kV-switching in dual energy CT using a pre-reconstruction decomposition technique. In *Medical Imaging 2008: Physics of Medical Imaging*, volume 6913, page 691313. International Society for Optics and Photonics, 2008.